The Meteoritical Society

Meteoritics & Planetary Science 1–20 (2017)
doi: 10.1111/maps.13006

Experimental shock metamorphism of terrestrial basalts: Agglutinate-like particle formation, petrology, and magnetism

Dmitrii D. BADYUKOV[1], Natalia S. BEZAEVA[2,3,*], Pierre ROCHETTE[4], Jérôme GATTACCECA[4], Joshua M. FEINBERG[5], Myriam KARS[6], Ramon EGLI[7], Jouko RAITALA[8], and Dilyara M. KUZINA[3]

[1]V.I. Vernadsky Institute of Geochemistry and Analytical Chemistry, Russian Academy of Sciences, 19 Kosygin str., 119991 Moscow, Russia
[2]Institute of Physics and Technology, Ural Federal University, 19 Mira Str., 620002 Ekaterinburg, Russia
[3]Institute of Geology and Petroleum Technologies, Kazan Federal University, 4/5 Kremlyovskaya Str., 420008 Kazan, Russia
[4]Aix-Marseille Université, CNRS, IRD, Coll. France, CEREGE, 13545 Aix en Provence, France
[5]Institute for Rock Magnetism, University of Minnesota, 116 Church Street SE, Minneapolis, Minnesota 55455, USA
[6]Center for Advanced Marine Core Research, Kochi University, B200 Monobe, Nankoku 783-8502, Japan
[7]Central Institute for Meteorology and Geodynamics, Hohe Warte 38, 1190 Vienna, Austria
[8]Astronomy Department, University of Oulu, P.O. Box 8000, FI-90014 Oulu, Finland
[*]Corresponding author. E-mail: bezaeva@gmail.com

(Received 23 February 2017; revision accepted 28 September 2017)

Abstract–Hypervelocity impacts occur on bodies throughout our solar system, and play an important role in altering the mineralogy, texture, and magnetic properties in target rocks at nanometer to planetary scales. Here we present the results of hypervelocity impact experiments conducted using a two-stage light-gas gun with 5 mm spherical copper projectiles accelerated toward basalt targets with ~6 km s^{-1} impact velocities. Four different types of magnetite- and titanomagnetite-bearing basalts were used as targets for seven independent experiments. These laboratory impacts resulted in the formation of agglutinate-like particles similar in texture to lunar agglutinates, which are an important fraction of lunar soil. Materials recovered from the impacts were examined using a suite of complementary techniques, including optical and scanning electron microscopy, micro-Raman spectroscopy, and high- and low-temperature magnetometry, to investigate the texture, chemistry, and magnetic properties of newly formed agglutinate-like particles and were compared to unshocked basaltic parent materials. The use of Cu-projectiles, rather than Fe- and Ni-projectiles, avoids magnetic contamination in the final shock products and enables a clearer view of the magnetic properties of impact-generated agglutinates. Agglutinate-like particles show shock features, such as melting and planar deformation features, and demonstrate shock-induced magnetic hardening (two- to seven-fold increases in the coercivity of remanence B_{cr} compared to the initial target materials) and decreases in low-field magnetic susceptibility and saturation magnetization.

INTRODUCTION

Bombardment of cosmic bodies represents an agent responsible for soil formation on the surfaces of airless solid solar system bodies. Bombardment intensity controls such surface processes as degree of comminution of solid surface rocks, rates of regolith growth and gardening, and mineralogy together with physical and mechanical properties of regolith.

According to high-resolution images, surfaces of many asteroids are covered by regolith (e.g., Garcia et al. [2015] and references therein). However, to date,

aside from regolith breccia meteorites (Bischoff et al. 2006) and regolith samples from the asteroid 25143 Itokawa collected by the Hayabusa mission (Noguchi et al. 2014) that we do not discuss here, lunar regolith is the only example of regolith available for a broad spectrum of laboratory studies.

Both large crater-forming bodies (>10 m) and small particles (μm to mm) contribute to the formation and reworking of regolith, whereas contribution of intermediate-sized projectiles to the surface processing is virtually negligible. Indeed, the micrometeoroid flux in the vicinity of the Earth was estimated as $(40 \pm 20) \times 10^6$ kg yr^{-1} to its surface (Love and Brownlee 1993) and the flux of crater-forming extraterrestrial bodies ranging in size from ~10 m to ~2 km was estimated as ~40×10^6 kg yr^{-1} (Kyte and Wasson 1986). Both fluxes are of the same order of magnitude, whereas the flux of intermediate-sized bodies (~4 mm to 10 m in size) to the Earth is only ~0.28×10^6 kg yr^{-1} (Kyte and Wasson 1986). The calculated average micrometeoroid impact velocity on the Moon is 15.3 km s^{-1} (Cremonese et al. 2013) and the root-mean-square impact velocity of crater-forming bodies is 19.2 km s^{-1} (Stuart and Binzel 2004). Hence, if the flux of micrometeoroids on the Moon is roughly equal to the flux of crater-forming bodies ranging in size from ~10 m to ~2 km (as on Earth), and the micrometeoroid velocity distribution spectrum for micrometeoroids is similar to the spectrum for crater-forming objects, then we could expect that these two suites of projectiles contribute an equal amount of impact energy to the Moon's surface.

Lunar regolith has been extensively investigated in the past (e.g., Heiken et al. 1991; Basu et al. 2002; Korotev et al. 2010). The fraction of lunar regolith with sizes <~1 mm, known as lunar soil, consists mainly of lithic and mineral clasts, different breccias, impact glasses, and agglutinates (Heiken et al. 1991). It is believed that impact glasses and agglutinates were mainly or entirely formed as a result of crater-forming events and micrometeorite impacts, respectively (Heiken et al. 1991).

It was shown that the Apollo 16 soil contains 14% of impact glasses and 16% of agglutinates (Korotev et al. 2010), which demonstrates that the contribution of micrometeoroid bombardment to regolith evolution is comparable to corresponding contribution of crater-forming events, forming agglutinates and glasses, respectively. The main consequence of the micrometeoroid impacts is agglutination or, in other words, formation of clastic detritus bonded by glass, agglutinates. The fusion of the finest fraction (F^3) model (Papike 1981) has been widely accepted for the origin of agglutinitic glass. It was previously reported that agglutinate-type glasses are produced via impacts on solid targets at impact velocities >5 km s^{-1} (Hörz et al. 1975; Hörz and Schaal 1981).

Agglutinate-like particles have been produced in shock-recovery experiments using the Vertical Impact Facility in laboratory conditions from solid targets by repetitive impacts of stainless steel or Ni-alloy projectiles (Cintala et al. 1984; See and Hörz 1988). They are characterized by preferential melting of plagioclase and differ from lunar agglutinates by more heterogeneous composition of glasses. In spite of previous efforts to produce agglutinate-like particles in laboratory conditions, previous authors did not quantify the projectile matter in agglutinate-like particles nor characterized their magnetic properties. Moreover, magnetic projectiles made of iron or Ni-alloy contaminate the target by additional ferromagnetic matter, and thus, obscure any shock-induced changes in the magnetic properties of the target material itself.

We conducted a set of shock-recovery experiments using a gas gun and bulk basalt targets of different origin together with copper projectiles 5 mm in diameter, sent to the target with impact velocities of about 6 km s^{-1}. We report here shock-induced agglutinate-like particle formation and address both petrology and chemistry of particles including estimations of projectile matter quantity in the particles and evaluation of shock metamorphism of clasts therein, as well as full magnetic characterization of these particles. Indeed magnetic properties are sensitive tracers of a variety of shock-induced phenomena: formation of nanometer-sized metallic iron particles, contamination by magnetic phases from the impactor, and changes in the intrinsic magnetic properties of the target rock by fracturing and damages in the original magnetic minerals (Morris and Gose 1976; Pesonen et al. 1997; Taylor et al. 2001; Bezaeva et al. 2016). This is exemplified by the lunar regolith where the concentration of agglutinates and the magnetic properties are well correlated (Rochette et al. 2010).

MATERIALS AND METHODS

Samples

Four types of natural basaltic rocks (1–4) were chosen for our shock-recovery experiments (further referred to as "lithologies"). Bulk density values for the chosen basalts as well as the correspondence between the type of basaltic target and shot number are presented in Table 1. Chemical compositions of the basalts are presented in Table 2.

1. Oceanic fine-grained basalt from the Mid-Atlantic Ocean Ridge (shot 9, see Table 1) displays a

Table 1. Main parameters of shock-recovery experiments.

Shot #	Basalt type	d, g cm^{-3}[a]	v, km s^{-1}	p, kPa	P, GPa
9	(1) Oceanic	2.9	6.02	5.3	108
12	(2) Olivine	3.0	5.42	4.5	91
13	(2) Olivine	3.0	5.94	4.7	105
18	(3) Aluminous	2.9	5.83	4.7	102
19	(3) Aluminous	2.9	6.04	3.7	108
25	(4) Tholeiitic	3.2	6.30	0.2	132
26	(3) Aluminous	2.9	5.82	1.9	102

[a]Basalt bulk density was determined by a volumetric technique with an accuracy of ±0.1 g cm^{-3}.
d = bulk density; v = projectile velocity; p = chamber's air pressure; P = peak shock pressure in GPa.

variolitic texture and consisted of rare olivine ($Fa_{15–20}$), augite ($Fs_{22–27}Wo_{43–45}$), and glass between plagioclase ($An_{65–75}$) laths. Titanomagnetite ($Fe_{3-x}Ti_xO_4$, $0 \le x \le 1$, abbreviated as Tmt) occurs as subhedral and euhedral 0.5–3 μm grains disseminated throughout the rock matrix; small crystal sizes prevented accurate microprobe analyses. Titanium contents (x) were calculated using thermomagnetic analyses and the relationships of Bleil and Petersen (1982) (see the Thermomagnetic Analyses section for details).

2. Olivine basalt (Kamchatka, Russia) (shots 12 and 13, see Table 1) consists of 0.1–0.3 mm microphenocrysts of olivine ($Fa_{16–20}$), plagioclase ($An_{70–75}$), and pyroxene ($Fs_{10}Wo_{46}$) in a fine-grained matrix with an intersertal texture. The matrix consists of ~40 μm crystals of plagioclase ($An_{65–75}$), subhedral and euhedral pigeonite ($Fs_{25}Wo_6$), augite ($Fs_{8–14}Wo_{39–44}$), and interstitial glass rich in submicrometer pyroxene grains. Two types of titanomagnetite grains occur: relatively large grains of 15–50 μm and smaller grains 1–3 μm in size, which border matrix pyroxene.
3. Aluminous basalt from Kamchatka (Russia) (shots 18, 19, and 26, see Table 1) shows a porphyritic texture composed of zoned, 0.5–1.0 mm plagioclase ($An_{42–71}$) and olivine ($Fs_{25–27}$) phenocrysts in a matrix with an intersertal texture. The matrix consists of plagioclase ($An_{55–73}$) with minor interstitial glass, and pyroxene ($Fs_{27–29}Wo_{10}$ and $Fs_{14–16}Wo_{53–61}$) grains contain olivine inclusions. Titanomagnetite occurs as both 5–40 μm euhedral grains and submicron crystals disseminated throughout the matrix.
4. Tholeiitic basalt (shot 25, see Table 1) from the Putorana (East Siberia, Russia) trap formation shows a doleritic texture of plagioclase ($An_{66–78}$), pigeonite ($Fs_{30–33}Wo_{19–13}$) and augite ($Fs_{14–16}Wo_{39–43}$) with occasional quartz. Grain sizes range from 0.1 to 1 mm. Microprobe analyses identified titanomagnetite and ilmenite (Table 2); the latter contains needle-like precipitates of rutile according to SEM data. These oxides mostly form aggregates of 20–60 μm. Thermomagnetic analyses indicated Ti-poor Tmt ($x < 0.1$) and pure magnetite (also confirmed by the results of low-temperature magnetometry, see below). The latter was not identified during microprobe analyses likely due to its nanometer-scale grain size.

Titanomagnetites from the basalt samples contain 5–20 wt% of TiO_2 with traces of Al_2O_3, MgO, CaO, SiO_2, and V_2O_3. The rocks were fresh and did not exhibit any traces of hydrothermal alteration or weathering. However, it is likely that analyzed Al, Si, Ca, and possibly Mg are not actually within titanomagnetite but results from the interference by neighboring silicates due to the small size of the analyzed crystals.

Shock Experiments

Our samples were shocked using a two-stage light-gas gun at the Institute of Mechanics (M.V. Lomonosov Moscow State University, Russia).

The target basalts were shaped in 10 cm high cylindrical blocks with 10 cm diameters. Each block was fixed in a target steel holder that was situated in a sample cell that prevented spreading of target debris outward into the gun chamber (Fig. 1a). Before the shot, the gun chamber was evacuated to air pressures between 0.2 and 5.3 kPa (Table 1). These experiments used spherical 5 mm in diameter copper projectiles that were launched by the light-gas gun at velocities of about 6 km s^{-1} (Fig. 1a; Table 1). The copper material contains minor amounts of Fe (0.7 wt%), Zn (0.2 wt%), and P (0.5 wt%). An example of basaltic target after shock is shown in Fig. 1b. Agglutinate-like particles were recovered after shock and are discussed below.

Peak Shock Pressure Estimations

Peak shock pressures (P) estimated at the projectile–target contacts and other parameters for our shock experiments are presented in Table 1. The shock pressures were calculated using the plane shock approximation and the impedance match technique. The shock adiabats (the Hugoniots) of copper and basalts (Ahrens and Johnson 1995a,1995b) were used under the assumption that the difference between the Hugoniots for the basalts used in our experiments and the Hugoniots after Ahrens and Johnson (1995b) is

Table 2. X-ray fluorescence bulk rock analyses (Bulk), average microprobe analyses of homogeneous melt glass (Glass), and representative EDS and microprobe analyses of iron oxides in the unshocked basalts; all in wt%.

	(1) Oceanic			(2) Olivine			(3) Aluminous			(4) Tholeiitic			
Basalt	Bulk	Glass[b] (n = 9, 1SD)	Mt[a]	Bulk	Glass[b] (n = 3, 1SD)	Mt[a]	Bulk	Glass[b] (n = 32, 1SD)	Mt	Bulk	Glass[b] (n = 5, 1SD)	Ilm	Mt
SiO_2	51.01	51.28 ± 0.81	2.3	53.38	51.75 ± 1.17	b.d.	54.04	54.74 ± 1.52	0.08	49.04	53.13 ± 0.70		1.23
TiO_2	1.69	1.50 ± 0.37	19.7	0.92	0.54 ± 0.24	13.1	1.15	1.24 ± 0.28	12.31	1.72	1.72 ± 0.46	47.62	6.94
Al_2O_3	15.51	15.95 ± 1.03	1.8	14.95	15.64 ± 1.28	2.3	18.24	17.13 ± 2.89	2.00	14.77	19.08 ± 1.44	0.16	0.69
Cr_2O_3	0.04	0.04 ± 0.03	b.d.	0.11	0.08 ± 0.03	b.d.	0.02	b.d.	b.d.	n.d.	b.d.	b.d.	0.07
V_2O_3	n.d.	b.d.	b.d.	n.d.	b.d.	1.1	n.d.	n.d.	0.77	n.d.	b.d.	0.66	1.27
FeO	9.78	9.02 ± 0.77	74.2	8.35	6.21 ± 0.81	82.2	8.46	8.34 ± 2.46	74.08	11.77	8.36 ± 1.35	46.92	81.04
MnO	0.12	0.17 ± 0.04	0.8	0.16	0.13 ± 0.04	b.d.	0.17	0.18 ± 0.06	0.67	0.17	0.12 ± 0.04	0.52	0.60
MgO	8.08	7.45 ± 1.11	0.6	9.30	12.01 ± 1.38	1.3	4.52	4.99 ± 1.43	3.53	6.22	4.96 ± 1.28	1.12	0.42
CaO	11.53	11.52 ± 1.02	0.6	9.37	10.79 ± 1.11	b.d.	8.02	7.53 ± 0.94	0.21	9.81	11.66 ± 1.28	0.19	0.34
Na_2O	2.76	2.79 ± 0.37		2.29	2.58 ± 0.24		3.1	4.42 ± 0.95		2.41	2.31 ± 0.50		
K_2O	0.14	0.07 ± 0.03		0.85	0.62 ± 0.21		1.16	1.15 ± 0.24		0.89	0.29 ± 0.26		
P_2O_5	0.11	0.14 ± 0.08		0.21	0.23 ± 0.07		0.23	0.36 ± 0.08		0.22	b.d.		
LOI	b.d.			b.d.			b.d.			2.50			
Total	100.62			99.89			99.64		93.71	99.57		98.70	92.60
x			0.53			0.35			0.35				0.21

[a]EDS analyses reduced to 100%.

[b]Microprobe homogeneous glass analyses were recalculated without Cu contents and reduced to 100%.

n = number of analyses; SD = standard deviation; n.d. = not determined; Mt = magnetite; Ilm = ilmenite; LOI = loss on ignition; b.d. = below detection; x = Ti content (a.f.u) in titanomagnetite $Fe_{3-x}Ti_xO_4$.

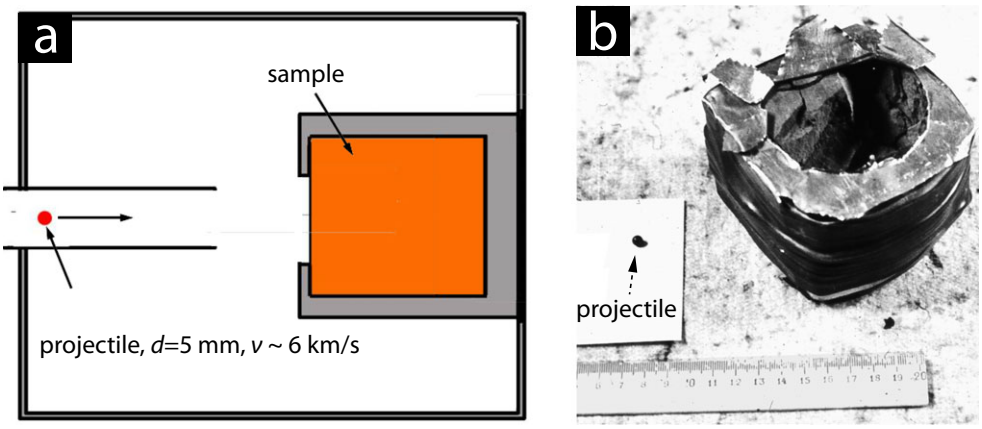

Fig. 1. a) Schematic drawing of a shock experiment; the sample is situated in the sample holder in a cell. b) Example of a basaltic target after shock (shot 9) and a copper projectile.

insignificant. The Hugoniot of a "low-density basalt" with the density of 2.793 g cm^{-3} and the Hugoniot of a "high-density basalt" with the density of 3.200 g cm^{-3} were applied for the used basalts with the densities of <3.0 and >3.2 g cm^{-3}, respectively. The Hugoniots are expressed as $U_s = 2.4 + 1.60U_p$ for $U_p > 2.1$ km s^{-1} and $U_s = 4.09 + 1.35U_p$ for $U_p > 1.913$ km s^{-1} for low- and high-density basalts, respectively, where U_s and U_p are shock and particle velocities. It should be noted that, as the target is a lot bigger than the projectile, these highest pressures encompass target volumes to be comparable with those of projectiles. By further propagation into a target, a shock wave attenuates and shock pressure drops to values ≤2 GPa at the rear side of the used targets according to calculations (Melosh 1989).

Instruments and Measuring Techniques

Whole-rock compositions of unshocked basalts were obtained using the X-ray fluorescence technique at the V.I. Vernadsky Institute RAS (Moscow, Russia). Particles with reddish color, commonly containing visible copper inclusions of projectile material and distinct from basalt clasts, were picked out from target debris after the shock experiments. Forty-four particles (approximately six particles per shot) were mounted into epoxy and thin-sectioned, whereas other particles were used for bulk magnetic measurements. Sectioned particles were examined using an optical microscopy and a JEOL 6400 scanning electron microscope equipped with an energy dispersive X-ray spectrometer (EDS) at the University of Oulu (Finland). Chemical compositions of particle components were obtained using JEOL JXA-8200 SuperProbe Electron Probe Microanalyzer (University of Oulu). Analyses were conducted using an accelerating voltage of 15 kV and a beam current of 10 nA. Detection limits are approximately 0.02 wt% for all elements. Glass areas were analyzed using a focused beam (1 μm in diameter). For the analyses, we chose areas without visible Cu droplets. Mineral and compound standards and the JEOL ZAF correction software were applied for data reduction.

Magnetic characterization was performed in four research centers: CEREGE (Aix-en-Provence, France); the Institute for Rock Magnetism (IRM) (Minneapolis, USA); the Center for Advanced Marine Core Research, Kochi University (Nankoku, Japan); and Kazan Federal University (KFU) (Kazan, Russia).

Low-field magnetic susceptibility (χ_0) and $\chi_0(T)$ up to 600 °C (one heating–cooling cycle under argon atmosphere) were measured using MFK1-CS3 AGICO apparatus at CEREGE (unshocked bulk samples) and KFU (unshocked samples crushed into powder), respectively. In-field thermomagnetic curves for unshocked bulk samples and the *25-s5* agglutinate-like particle were acquired under vacuum up to 600 °C (700 °C for *25-s5*) using a magnetic balance NMB-89 by Natsuhara-Giken at Kochi University with a 10 °C min^{-1} heating rate under 300 mT magnetic field.

The saturation isothermal remanent magnetization (SIRM) and its corresponding alternating field (AF) demagnetization spectra were measured at CEREGE using a 2G Enterprises SQUID (superconducting quantum interference device) cryogenic magnetometer, equipped with an inline AF demagnetizer. This magnetometer allows for the measurement of moments up to 10^{-4} Am^2 with a practical background noise level of 10^{-11} Am^2 and AF demagnetization up to fields of 150 mT. A 3T SIRM was imparted using a pulse magnetizer MMPM9 from Magnetic Measurements Ltd.

Low-temperature (5–300 K) magnetic measurements, including zero-field-cooled (ZFC)—field-cooled (FC) remanence and room-temperature SIRM (RT-SIRM) cooling–warming cycles, were collected using a Quantum Design Magnetic Property Measurement System (MPMS)-2 at the IRM and a Quantum Design MPMS-XL5 at Kochi University. The SIRM at 300 K and 5 K was imparted using a 2.5 T magnetic field. The same MPMS instruments were also used to measure the field amplitude and frequency dependencies, χ'_{fd} and χ''_{fd}, of in-phase (χ') and out-of-phase (χ'') components of magnetic susceptibility, respectively, in the 5–300 K range ($F1$ = 1 Hz, $F2$ = 10 Hz, $F3$ = 100 Hz, and B = 300 μT were used). Major hysteresis loops (with parameters such as saturation magnetization, M_s; saturation remanent magnetization, M_{rs}; coercivity, B_c) and back-field remanence demagnetization curves (with main parameters such as M_{rs} and coercivity of remanence B_{cr}) were measured for all samples at room temperature, using a Princeton Micromag Vibrating Sample Magnetometers (VSM) at CEREGE (with 1 T maximum applied magnetic field). Hysteresis loops and back-field remanence demagnetization curves were measured in high (up to 700 °C) and low (5–300 K) temperature ranges at the IRM. The same type of VSM was used at Kochi University to acquire raw first-order reversal curve (FORC) data. FORC distributions were calculated using the VARIFORC protocol of Egli (2013) within the FORCinel software of Harrison and Feinberg (2008), with typical smoothing values of Sc0 = 4, Sb0 = 3, Sc1 and Sb1 = 7, and vertical and horizontal lambda values of 0.1.

RESULTS

Petrographic Effects of Shock: Texture of Agglutinate-Like Particles

The target cylinders all displayed deep cavities after the shock experiments were complete (Fig. 1b). Cavity sizes were approximately 8 cm in diameter and 6–8 cm in depth. The comminution products were found mostly out of the cavities in the sample cell (Fig. 1), although some fraction of debris was present within the cavities. The target fragments range in size from a few cm to a few μm or less.

Small (0.3 to 5–6 mm) particles were found among the debris (Fig. 2)—these particles are the main focus of this work. The particles are distinguished among target fragments by their reddish color and were picked out using a binocular microscope. The rest of the debris (not investigated here) occurs as crushed target material without any visible traces of shock-induced alteration—melting or changing in the color. The recovered mass of particles from each shot was approximately 1 g or less. Figure 2a displays a particle of a typical shape. It is seen in Fig. 2a that the particle is covered by strongly adhered basaltic dust. The image at greater magnification (Fig. 2b) illustrates agglutinate-like particle surface details. Smooth areas of particle surface are composed of silicate glass with tiny copper grains (see tiny spheres in Fig. 2b); the unmelted basalt clasts are also exposed at the surface. Particles' internal texture (Fig. 2c) is characterized generally by rock and mineral clasts mixed with melt glasses and projectile matter and is not variable between the particles from different shots. Texturally, the particles are very similar to the agglutinate-like particles produced in previous experiments (See and Hörz 1988; Hörz and Cintala 1997). Accordingly, we also refer to our particles as "agglutinate-like particles."

Two types of glasses could be distinguished in the particles (Fig. 2d). The first glass type is quite homogeneous chemically ("G_{hm}" on Figs. 2d and 2e). It contains numerous copper spheres and droplets disseminated in a porous silicate matrix. The size of copper inclusions ("Cu" on Figs. 2c–e) ranges from <1 μm up to ~0.6 mm with an average of 10–80 μm. The second glass type is in the form of heterogeneous glass ("G_{htr}" on Figs. 2d and 2e) such as the inclusions with different backscatter electron (BSE) contrast (Fig. 2d). The rounded glass inclusions have a flow-banded or patched structure and are usually situated in a matrix consisting of the homogeneous glass with numerous projectile droplets (Fig. 2d). The particles sometimes contained relatively large irregularly shaped nuggets of copper. Compositions of the glass band patches are similar to compositions of plagioclase and/ or/ pyroxene ("Px" on Fig. 2e). This glass type does not contain projectile matter. The homogeneous glass is often observed cementing areas or fragments of heterogeneous glass.

Basaltic clasts are either unmelted ("C_{um}" on Fig. 2e) or partially melted ("C_{pm}" on Fig. 2c). In the latter case, plagioclase is converted to a slightly porous melt glass, whereas there are both unmelted and melted pyroxene (Figs. 2c and 2e). Unmelted basaltic clasts in agglutinate-like particles display shock effects that were observed using an optical microscope. The main shock effect is the formation of plagioclase diaplectic glass ("G_{dPl}" on Fig. 2e). We observed diaplectic glass as an isotropic phase of plagioclase compositions that does not show any signs of flow, without vesicles, and is situated in clasts that totally preserve the intact basaltic textures. Plagioclase in unmelted basaltic clasts in agglutinate-like particles from shots 9, 12, 18, and 25 are entirely converted into diaplectic glass, whereas plagioclase grains in clasts in particles from shot 13 are

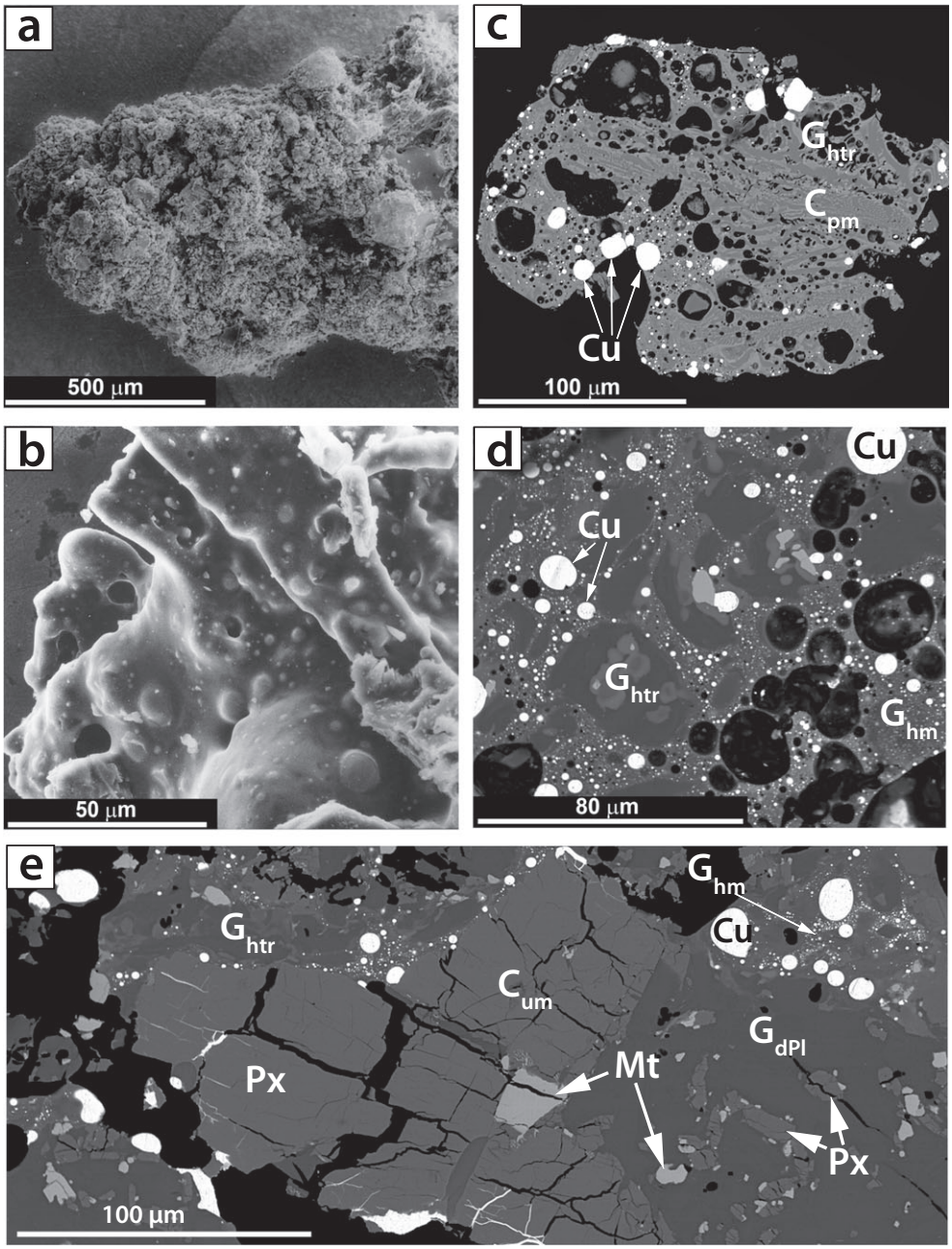

Fig. 2. a) Secondary electron (SE) image of agglutinate-like particle (shot 19, see Table 1). The particle surface is covered by strongly adhered basaltic dust. b) SE image of agglutinate-like particle surface details (shot 9); the surface is partially covered by a glass film; numerous knobs are copper droplets in the glass. c) Backscatter electron (BSE) image of the section of particle *9-s3* from shot 9 (see Table 1). The particle is composed of partially melted basaltic clasts (C_{pm}; the clasts are composed of a plagioclase melt glass and both melted and unmelted pyroxene) in a porous glassy matrix with disseminated copper droplets (white); partially melted clasts preserved in some parts the original texture; heterogeneous glass (G_{htr}) is present. d) BSE image of a fragment of agglutinate-like particle *26-s3* from shot 26 (Table 1). Inclusions of the heterogeneous glass (dark gray areas of different gradation with no white copper droplets) are embedded in the homogeneous glass (G_{hm}) with numerous copper droplets (Cu). e) Mosaic image of a fragment of particle *18-2* (shot 18) consisting of an unmelted basalt clast (C_{um}) in heterogeneous and homogeneous glasses. The clast is composed of pyroxene (Px), plagioclase diaplectic glass (G_{dPl}), and magnetite (Mt).

converted to diaplectic glass either entirely or partially. In the latter case, the planar deformation features (PDF) were present in the birefringed areas occupied by fractions of the grains. A few basaltic clasts in particles from shot 26 contain plagioclase grains with PDF and plagioclase in one clast is

Table 3. Characteristics of agglutinate-like particles.

Shot # (*n*)	Average projectile content (its range), vol%[a]	Average melt glass content (its range), vol%[a]	Range of porosity, vol%	State of Pl phases in unmelted clasts
9 (4)	6.5 (4.0–9.0)	55 (40–80)	10–30	dia.glass[b]
12 (3)	10.0 (5.0–18.5)	45 (40–50)	20–40	dia.glass
13 (3)	4.5 (2.0–5.5)	55 (40–65)	25–35	dia.glass, diaPl[b]
18 (4)	11.0 (10.5–11.5)	25 (20–30)	20–30	dia.glass
19 (3)	11.0 (9.0–13.5)	25 (10–40)	15–40	dia.glass
25 (4)	10.0 (3.5–21.5)	55 (45–65)	20–50	dia.glass
26 (3)	10.5 (6.0–14.5)	45 (20–60)	15–20	dia.glass, diaPl, Pl[b]

[a]Cu projectile and melt glass contents in agglutinate-like particles are given relative to the whole projectile–silicate fraction without taking into account the porosity.
[b]dia.glass = diaplectic glass; diaPl = diaplectic plagioclase with planar deformation features (PDF) and lowered birefringence; Pl = plagioclase without shock effects.
n = number of analyzed particles.

converted to diaplectic glass, whereas plagioclase grains in other clasts do not show any shock effects. The majority of pyroxene grains have polysynthetic mechanical twins absent in the intact material. Iron oxides ("Mt" on Fig. 2e) do not show any optically prominent features relating to shock metamorphic effects. The pressure histories of unmelted clasts in separate particles may be different (e.g., clasts can be shocked at different pressures). However, we can constrain the ranges of shock pressures for clasts in each shot. In accord with shock experiments with basalts and feldspars (Schaal et al. 1979; Ostertag 1983), we estimate that unmelted basaltic clasts in particles from shots 9, 12, 18, 19, and 25 were shocked at peak pressures ≥~30 GPa, ≥~25 for shot 13, and ≤~30 GPa for shot 26. Some characteristics of the agglutinate-like particles including contents of the projectile material and melt glass obtained via composite BSE images are presented in Table 3.

The chemically homogeneous glasses have compositions roughly similar to those of the initial basalts (Table 2; Fig. 3). The agglutinate glasses from shots 9, 18, and 26 show enrichment in P. There are no data on phosphorus content in glasses from shot 19; otherwise elemental composition of glasses from shot 9 approximately corresponds to the bulk initial basalt composition; the same applies to glasses from shot 26 (with an exception of enrichment in Na). The agglutinate glasses from shot 18 are richer in Ti, Mg, Fe, and Mn and poorer in K and Na relative to the initial basalt, whereas the glasses from shot 19 demonstrate some Mg and Fe depletion and K and Na enrichment relative to the initial basalt bulk composition. We suggest that these deviations are connected with an initial target heterogeneity—different proportions of constituent minerals (plagioclase and pyroxene) at the localized areas of projectile contact, i.e., the projectile in shot 18 impacted an area richer in pyroxene, whereas the impact area in shot 19 was richer in plagioclase.

Compositions of the chemically heterogeneous glasses on ternary plot Ca-Al-Fe+Mg (Fig. 4) correspond to both compositions of minerals and compositions of their mixtures. In the latter case, the glass compositions show a mix of plagioclase with pyroxenes due to higher abundances of plagioclase and pyroxenes relative to olivine in the rock.

A noteworthy geochemical observation is the presence of Cu in the shocked materials. Microprobe analyses of homogeneous "whole rock" glasses performed on areas without visible projectile droplets show Cu concentrations from 1.5 wt% up to, maybe, 10 wt%. However, it is possible that the highest Cu concentrations may be due to Cu droplets underlying a surface and their interaction with an electron beam. More intriguing is the presence of Cu in minerals from unmelted basalt clasts and heterogeneous glasses (Fig. 5), which do not show any visible traces of contamination by copper projectile material. Cu concentrations in olivine, pyroxene, plagioclase, and heterogeneous glasses range from detection limit (0.02 wt%) to ~2 wt% with average concentrations of 0.59, 0.40, 0.48, and 0.74 wt%, respectively. There is no systematic difference in the Cu contents in silicates from the agglutinate-like particles from different shots. In order to exclude the possibility of copper smearing on mineral surfaces by polishing, we made a slide consisting of a mixture of unshocked basaltic grains with Cu particles. Microprobe data show a presence of Cu in the mineral analyses but the Cu concentrations did not exceed 0.07 wt%. Ten-minute etching of polished surfaces of studied sections in an HNO_3–HCl mixture (aqua regia) also did not change the

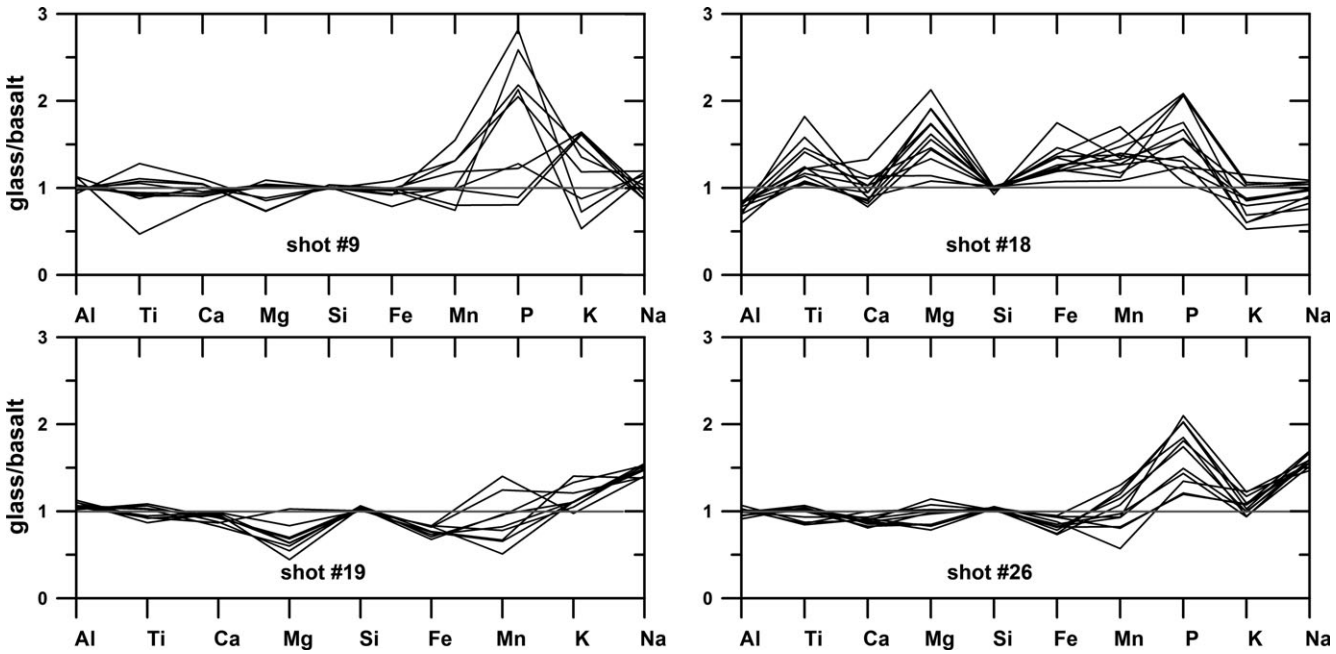

Fig. 3. Individual analyses of homogeneous agglutinate glasses normalized to the composition of precursor basalts. For shot 19, phosphorus contents were not measured.

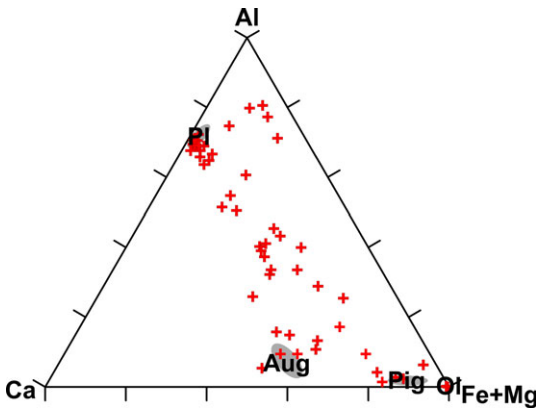

Fig. 4. Compositions of minerals and individual analyses (crosses) of heterogeneous glasses produced in experiments and plotted on ternary Ca-Al-Fe+Mg (at.) diagram. The major basalt minerals are plagioclase (Pl), augite (Aug), pigeonite (Pig), and olivine (Ol). Their compositions vary in all used basalt types in narrow ranges marked by the gray areas on the diagram. Individual analyses of heterogeneous glasses reveal variable mixtures of mineral melts as well as clustering about the plagioclase composition.

Cu contents in the minerals from the agglutinate-like particles.

Rock Magnetic Effects of Shock: Magnetic Properties of Unshocked Basalts and Agglutinate-Like Particles

Main rock magnetic properties of unshocked basaltic samples and corresponding agglutinate-like particles (discussed below) are presented in Table 4.

Thermomagnetic Analyses of Initial Basalts and an Agglutinate-Like Particle

Thermomagnetic analyses of rocks are often used to identify the composition of constituent magnetic minerals (Ti-constituent and Ti-free magnetite for this study) via determination of their Curie temperatures (T_c). We acquired induced magnetization versus temperature $M_s(T)$ data for all four lithologies (Fig. 6) and estimated T_c from the corresponding heating curves using the two-tangent method (Grommé et al. 1969), which was then converted into titanium content x in the titanomagnetite using the relationship of Bleil and Petersen (1982).

Sister samples of unshocked basalt display similar looking M_s–T curves, suggesting a relatively homogeneous magnetic mineral assemblage in the preshocked material. There are some notable differences between basalts from different shots (e.g., shots 18, 19, and 26, see below), reflecting normal magnetic variability in basalts.

Major T_c for the oceanic basalt (1st lithology, shot 9, Fig. 6a) is 180 °C ($x = 0.59$), although additional minor peaks of the heating curve and its long "tail" may be indicative of heterogeneous Tmt composition. Thermomagnetic analyses for unshocked samples from the olivine basalt (2nd lithology, i.e., shots 12 [Fig. 6b] and 13) reveal T_c = 518–520 °C, which points to Ti-poor magnetite with $x = 0.10$. Initial basaltic samples

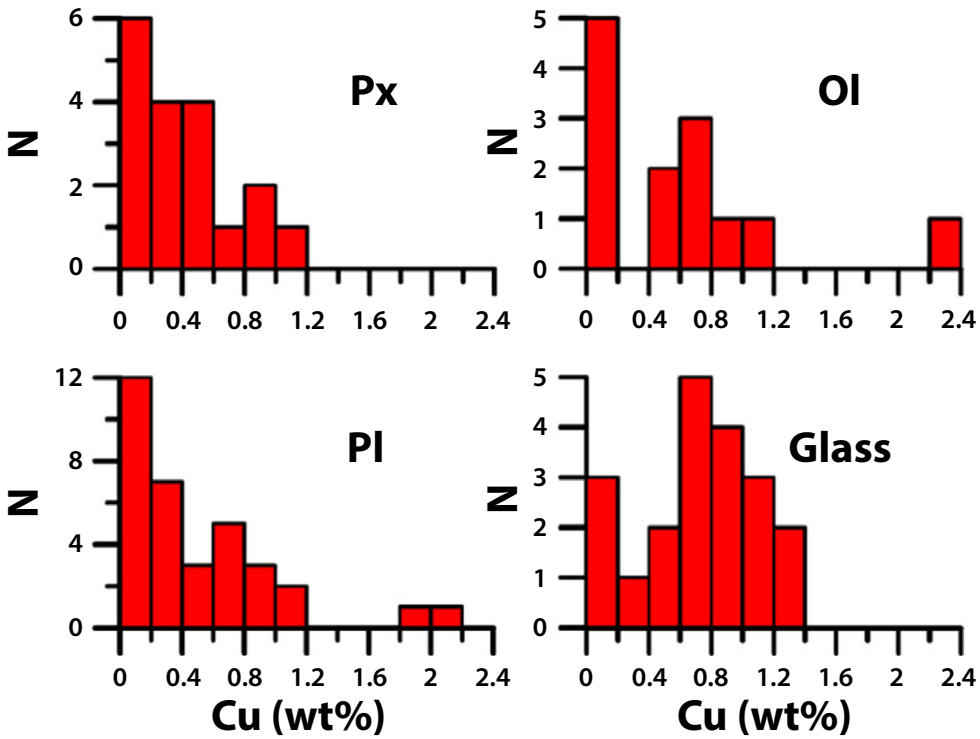

Fig. 5. Cu concentrations in pyroxene (Px), olivine (Ol), and plagioclase (Pl) grains from shocked unmelted basaltic clasts in agglutinate-like particles and in heterogeneous glasses (Glass). *N* is the number of analyses.

from the aluminous basalt (3rd lithology) demonstrate T_c = 452 °C ($x \sim 0.21$) for shot 18 (Fig. 6c), T_c = 419 °C ($x \sim 0.26$) for shot 19, and T_c = 338 °C ($x \sim 0.38$) for shot 26 indicating some heterogeneities in Tmt composition within different blocks of the same lithology. Analyses of the heating curve $M_s(T)$ for initial basaltic sample from shot 25 (tholeiitic basalt, 4th lithology) point out to Ti-poor magnetite with $x < 0.10$ (T_c = 569 °C), although temperature dependence of low-temperature magnetic susceptibility χ_0-T reveals Ti-free magnetite Curie point of 580 °C. Ti-free magnetite in the tholeiitic basalt was independently confirmed with low-temperature magnetometry via its characteristic Verwey transition (Verwey 1939) (see below).

In order to assess the possibility of shock-induced formation of new magnetic minerals, we conducted an additional set of thermomagnetic analyses on the agglutinate-like particle *25-s5* from shot 25 (tholeiitic basalt target). $M_s(T)$ up to 700 °C for *25-s5* looks very similar to the corresponding $M_s(T)$ for the precursor tholeiitic basalt (Fig. 6d) and displays only a magnetite Curie temperature. There is no signal at 700 °C, which excludes the possibility of shock-induced formation of significant amount of metallic iron (with T_c = 768 °C).

Magnetic Hysteresis and First-Order Reversal Curves

The average magnetic domain state of the shocked and unshocked samples can be estimated using a plot of M_{rs}/M_s versus B_{cr}/B_c, often referred to as a "Day plot" (Day et al. 1977; Dunlop 2002) (Fig. 7).

As seen from Fig. 7 and Table 4, all samples before and after shock roughly fall into pseudo-single-domain (PSD) magnetic grain size range. Moreover, aside from sample 9, there is a systematic shift of all shocked samples (agglutinate-like particles) toward higher coercivity, single-domain (SD)-like behavior, when compared to the corresponding unshocked precursors. This shock-induced enhanced coercivity is consistent with previous findings (e.g., Bezaeva et al. [2016] and references therein), and may be due to domain wall pinning, microcracking, and/or fragmentation of magnetic grains (Bezaeva et al. 2016). On the other hand, we cannot exclude that new SD grains have nucleated independently from the melt while primary volcanic oxides have not been entrained in the melt or been fully melted. However, this hypothesis cannot be tested with EDS mapping as the critical SD size for magnetite and Ti-magnetite is below the spatial resolution of the electron microscope ($\ll$1 μm: it is estimated to be 0.05–0.084 μm for Ti-free magnetite and 0.2 μm for Tmt with x = 0.55–0.6 [Dunlop and Özdemir 1997]).

Table 4. Some characteristics of initial (unshocked) basalts and the corresponding agglutinate-like particles.

Shot # (n)	m	χ_0[a]	SIRM[a]	M_s[a]	M_{rs}/M_s	B_c	B_{cr}	B_{cr}/B_c
9 (3)	284 ± 35	2.9	130 ± 2	0.37	0.356 ± 0.013	10	14	1.4
9s (1)	24	0.7, 1.4	50, 93	0.12, 0.21	0.441	62	99	1.6
12 (3)	272 ± 40	7.7 ± 0.1	201 ± 1	1.10 ± 0.01	0.197 ± 0.004	15	36	2.4
12s (1)	215	1.1, 2.0	70, 129	0.05, 0.09	0.360	40	62	1.6
13 (3)	193 ± 44	7.3 ± 0.2	183 ± 14	1.02 ± 0.04	0.186 ± 0.012	15 ± 1	38 ± 2	2.6 ± 0.1
13s (2)	111 ± 62	1.7 ± 0.8, 3.2 ± 1.4	122 ± 50, 244 ± 92	0.75 ± 0.26, 1.37 ± 0.47	0.363 ± 0.078	40 ± 2	62 ± 4	1.6 ± 0.1
18 (3)	254 ± 39	23.8 ± 0.4	257 ± 40	2.10 ± 0.08	0.123 ± 0.017	7 ± 1	18 ± 2	2.6 ± 0.3
18s (3)	55 ± 26	5.7 ± 2.2, 10.7 ± 4.2	593 ± 266, 1105 ± 497	1.46 ± 0.64, 2.73 ± 1.18	0.418 ± 0.024	43 ± 3	63 ± 2	1.5
19 (3)	265 ± 35	19.8 ± 0.3	215 ± 46	1.69 ± 0.12	0.127 ± 0.022	5 ± 1	13 ± 2	2.6 ± 0.2
19s (2)	63 ± 30	1.5 ± 0.1, 2.8 ± 0.1	149 ± 3, 201 ± 6	0.40 ± 0.02, 0.71 ± 0.01	0.419 ± 0.009	50 ± 3	80 ± 4	1.6
25 (3)	214 ± 60	6.5 ± 0.1	300 ± 10	1.07 ± 0.02	0.281 ± 0.011	34 ± 2	108 ± 4	3.2
25s (2)	55 ± 7	0.6 ± 0.2, 1.1 ± 0.3	22 ± 6, 39 ± 10	0.10 ± 0.02, 0.18 ± 0.03	0.229 ± 0.006	24 ± 1	47 ± 1	2.0
26 (3)	250 ± 27	17.7 ± 0.3	271 ± 101	1.68 ± 0.16	0.151 ± 0.039	8 ± 2	17 ± 4	2.3 ± 0.1
26s (3)	116 ± 22	3.0 ± 0.7, 5.6 ± 2.1	274 ± 52, 512 ± 98	0.64 ± 0.11, 1.19 ± 0.20	0.415 ± 0.007	44 ± 2	64 ± 3	1.5

[a]Agglutinate-like particles contain up to y = 44–46 wt% of Cu. The indicated mass (m) is the total mass (basalt target + incorporated Cu); mass-normalized values are normalized on m (lower value) and $m_1 = (100 - y) \times m$ (upper value), separated by ",". The ranges of mass-normalized values in the χ_0, SIRM, and M_s columns represent closed intervals covering the uncertainty in determination of mass of incorporated Cu.

Each number in the "Sample ID" column corresponds to a particular shot (see Table 1); "*s*" after shot number is for "shocked" and designates agglutinate-like particle; n is number of samples; m is mass (in mg); χ_0 is low-field magnetic susceptibility (in 10^{-6} m^3 kg^{-1}); SIRM is isothermal remanent magnetization (in mAm^2 kg^{-1}); M_s is saturation magnetization (in Am^2 kg^{-1}); M_{rs} is saturation remanent magnetization; B_c is coercivity (in mT); B_{cr} is coercivity of remanence (in mT).

As follows from Table 4, with one exception (shot 25), all shocked samples—agglutinate-like particles—are magnetically harder than the corresponding unshocked samples. The saturation magnetization (M_s) of the unshocked target basalts is ~2 to >10 times higher than M_s values for corresponding agglutinate-like particles (the indicated uncertainty is related to the unknown Cu concentration, see Table 4). Similarly, there is a corresponding shock-induced decrease in magnetic susceptibility (Table 4).

FORC distributions provide information about the distribution of microscopic coercivities within a sample and magnetic interactions between domains within magnetic mineral assemblages. Room-temperature FORC diagrams from the samples of all four unshocked lithologies and their corresponding agglutinate-like particles are presented in Fig. 8.

The FORC distribution for sample 9 of oceanic basalt (Fig. 8a) suggests a majority of the magnetic mineral assemblage is PSD magnetic grains (Dunlop and Özdemir 1997), consistent with direct observations and bulk hysteresis properties (Fig. 7; Table 4). Figure 8c displays a FORC distribution for the 2nd lithology (olivine basalt, unshocked sample 12; sample 13 has very similar FORC distribution), which suggests a mixture of SD, PSD, and MD magnetic grains, consistent with direct observations. The FORC distribution for the 3rd lithology (aluminous basalt, sample 18) is presented in Fig. 8e. It is characteristic of SD and PSD mixture. FORCs for unshocked samples 19 and 26 from the same lithology demonstrate the same features. The 4th lithology (tholeiitic basalt, sample 25) is characterized by PSD magnetic grains as well (Fig. 8g), consistent with bulk hysteresis parameters (Table 4) and direct SEM observations. FORC diagrams further illustrate a clear shock-induced magnetic hardening (and shock-induced magnetic softening for the 4th lithology, shot 25), which will be discussed below. It is worth mentioning that the vertical spread of the FORC distributions is wider in the shocked material than in the unshocked material (Fig. 8), which could be interpreted as evidence of increased magnetostatic interactions between magnetic particles.

Low-Temperature Magnetometry

ZFC-FC experiments, RT-SIRM cooling–warming cycles, and measurements of magnetic susceptibility as a

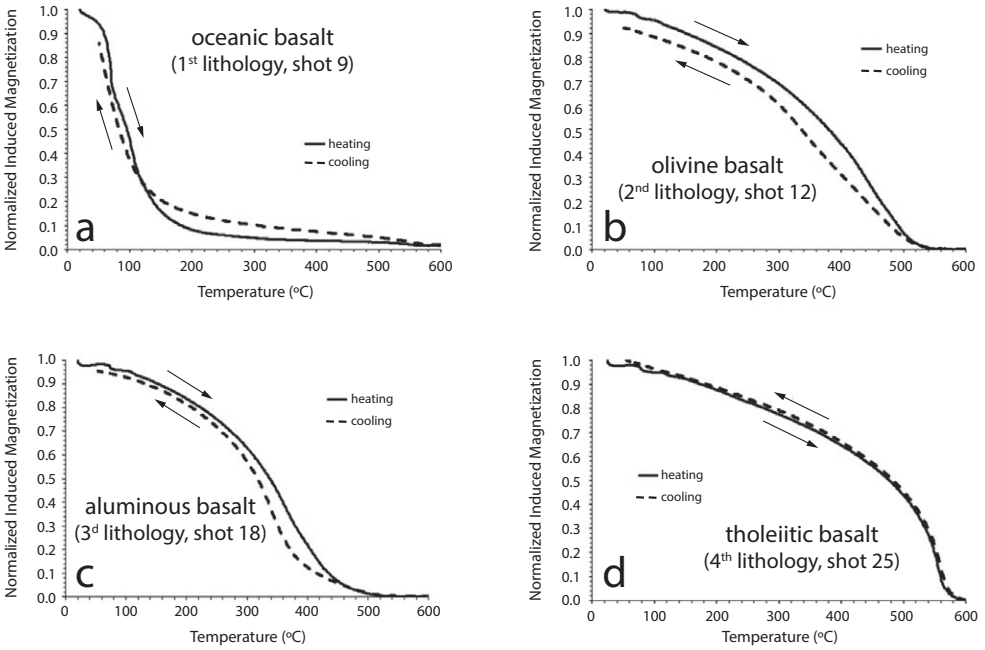

Fig. 6. In-field thermomagnetic curves $M_s(T)$ acquired under vacuum for (a) oceanic basalt (shot 9); (b) olivine basalt (shot 12); (c) aluminous basalt (shot 18); and (d) tholeiitic basalt (shot 25). Solid lines indicate heating cycles and dashed lines indicate cooling cycles (also indicated by the corresponding arrows). See Table 1 for details.

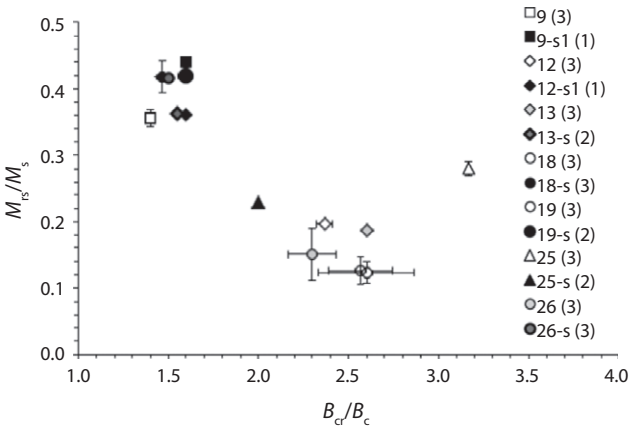

Fig. 7. Day plot showing M_{rs}/M_s versus B_{cr}/B_c for the unshocked samples used in all seven shots (Table 4) as well as for agglutinate-like particles from each shot (indicated by "*s*" for shocked). Number in parentheses corresponds to the number of used samples (in this case corresponding average value with $x - y$ standard deviations is plotted). All unshocked samples and agglutinate-like particles fall within pseudosingle-domain magnetic grain size range (Day et al. 1977; Dunlop 2002).

function of frequency were collected for both unshocked samples and agglutinate-like particles. These measurements are routinely used to detect magnetite via its characteristic Verwey transition at ~120 K (Verwey 1939; Jackson et al. 2011) as well as superparamagnetic (SP) particles, possibly formed through the shock, via frequency dependence of magnetic susceptibility χ_0 (in particular the in-phase and out-of-phase components χ' and χ'', respectively). The upper SP grain size limit for equidimensional grains of magnetite and Tmt ($x = 0.55$–0.6) is 25–30 and 80 nm, respectively (Dunlop and Özdemir 1997).

Ti-free magnetite was identified via its characteristic Verwey transition only for the unshocked sample of the 4th lithology group (shot 25, Fig. 9a). The Verwey transition temperature (T_v), determined from the peak on the 1st derivative of the ZFC warming curve is 98 K. Surprisingly, no T_v could be identified in Cu-basalt particles from the same shot for reasons discussed below.

The Cu-basalt particles are characterized by a relatively large out-of-phase component of magnetic susceptibility over the 10–300 K range with a peak at ~20 K and a broad decay at higher temperatures. Earlier work by Bowles et al. (2009) showed that an increase in frequency dependence of magnetic susceptibility in the low-temperature range (5–300 K) may indicate the presence of SP grains. One evident feature is that frequency dependence of χ'' is a factor 10–25 larger than the corresponding parameters in the precursor basalt.

Van de Moortèle et al. (2007) in a study of highly shocked Martian olivines showed that the formation of SP particles might be shock-induced. Rochette et al. (2015) also evidenced abundant SP magnetite in natural

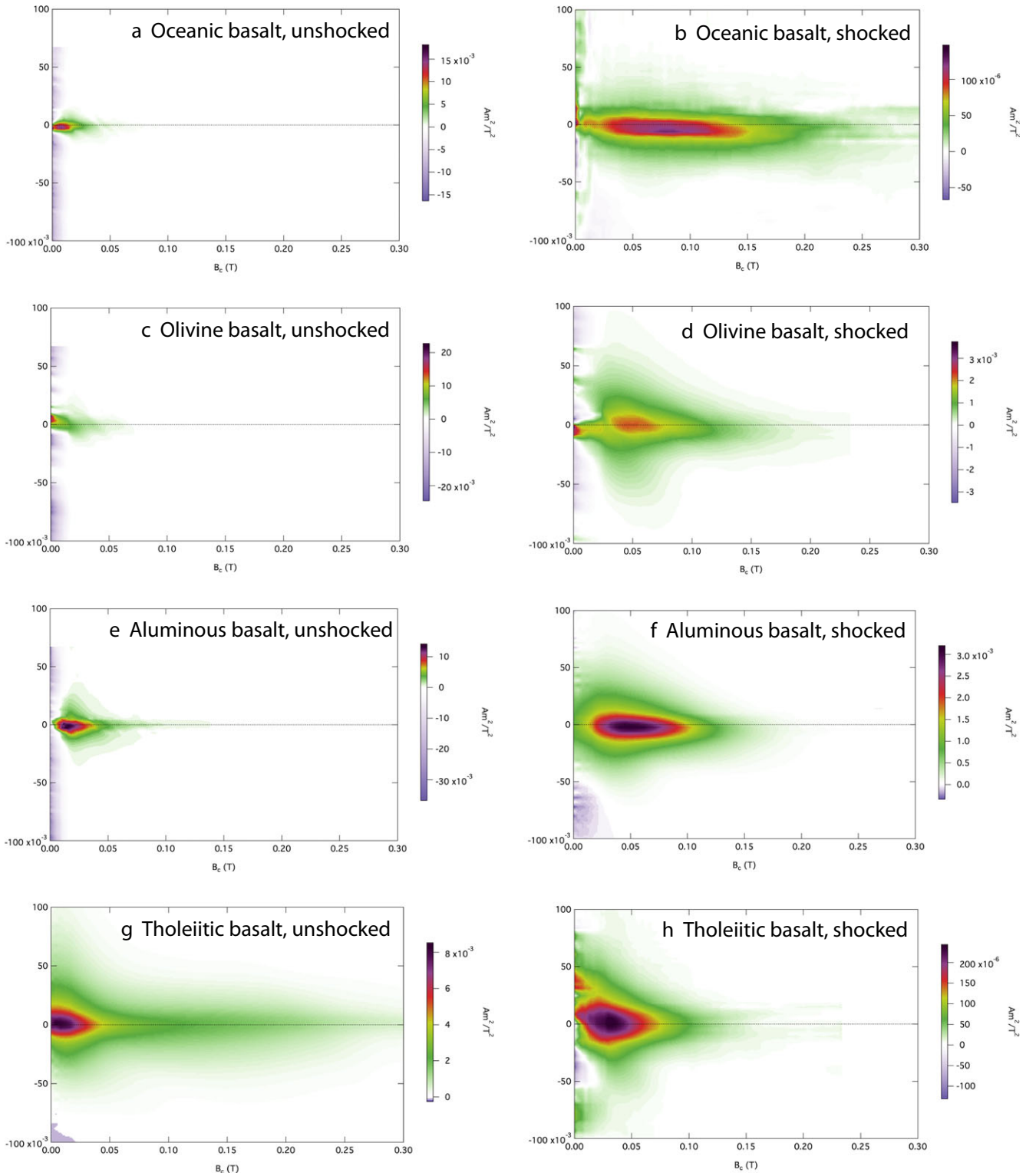

Fig. 8. First-order reversal curve (FORC) diagrams for unshocked basaltic samples and corresponding agglutinate-like particles. a) Unshocked sample 9 (lithology 1). b) Agglutinate-like particle 9-s1. c) Unshocked sample 12 (lithology 2). d) Agglutinate-like particle 12-s1. e) Unshocked sample 18 (lithology 3). f) Agglutinate-like particle 18-s3. g) Unshocked sample 25 (lithology 4). h) Agglutinate-like particle 25-s5. See Tables 1–4 for details.

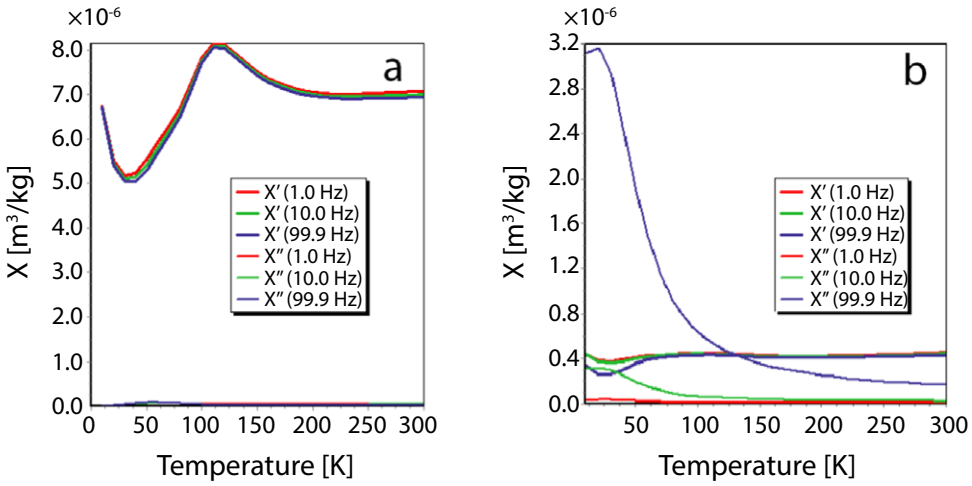

Fig. 9. MPMS susceptibility data set: frequency dependence of in-phase (χ') and out-of-phase (χ'') components of magnetic susceptibility between 5 and 300 K for (a) the unshocked basalt 25 and (b) the corresponding shock-induced agglutinate-like particle (Cu-basalt particle). Minor frequency dependence in (a) between 50 and 100 K is a known feature of multidomain titanomagnetite; it is related to rearrangement and localization of Fe^{2+}-Fe^{3+} cations within the domain walls (Carter-Stiglitz et al. 2006; Church et al. 2011). Major frequency dependence in (b), shown by the large out-of-phase component, is related to copper inclusions in the agglutinate-like particle (see text).

impact glasses. On the other hand, an increase in the out-of-phase susceptibility can also be explained by electrical eddy currents induced by the AC measurement field inside copper spherules, as this phenomenon is observed with AC measurements of good electric conductors (Worm et al. 1993; Bowles et al. 2009). In order to check whether the observed susceptibility features are due to shock-induced SP particles or the presence of copper in agglutinate-like particles, we simulated MPMS AC measurements for copper spherules with a mean radius of 40 μm (Fig. 10). The results of numerical modeling and MPMS AC measurements of copper standard for comparable frequencies of 40 and 140 Hz (Linford et al. [2002] and fig. 6d therein) confirm that the observed χ'_{fd} and χ''_{fd} are explainable by eddy currents inside the numerous copper droplets in Cu-basalt particles (up to 21.5 vol%, see Table 3), which were inherited from the projectile and thus should not be mistakenly interpreted as an evidence of shock-induced SP grains (compare Figs. 10b and 10c to Fig. 9b).

DISCUSSION

Formation of Agglutinate-Like Particles

As mentioned above, peak shock pressures reached at the projectile–target contacts in our experiments range from 91 to 132 GPa (Table 1). The postshock temperatures in Cu for pressures 90 and 130 GPa (McQueen and Marsh 1960) are approximately 550 °C and 950 °C, respectively. This is not sufficient for melting copper ($T_{melting}$ for copper is 1085 °C). Simplified calculations of postshock heating using a Mie–Grüneisen equation of state (Ahrens 1993) without taking into account phase transitions show that shock pressures of ~90 GPa cause complete melting of target basalts with temperatures of the melt exceeding ~1350 °C (up to 2450 °C for shot 25 with the contact pressure of 132 GPa). For the calculations we used approximate values of the enthalpy of basalt fusion of 400 kJ kg^{-1} and a specific heat of 1.3 kJ (kg^{-1} $°C^{-1}$) (Bouhifd et al. 2007). Ahrens and O'Keefe (1977) calculated a shock pressure of 52 GPa required for completely melting the gabbroic anorthosite taking into account phase transition in the rock. On the other hand, massive basalts experimentally shocked at 55 and 100 GPa contained ~5% and 40–80% of melt glass (Schaal et al. 1979). Somehow the maximum shock pressures at the contact zones were high enough to melt the targets due to a high postshock heating. Volume of the produced melt can be estimated as 1.5–2 volumes of the projectile (O'Keefe and Ahrens 1982). Using the maximum total weight of the particles (1.05 g, shot 26), their glass content (50%, Table 3), and a density of 3 g cm^{-3}, we can estimate a target melt volume of ~0.17 cm^3, which is close to a projectile volume of 0.2 cm^3. However, the volume of the projectile in all of the particles can be estimated at 0.035 cm^3, which corresponds to ~50% of a primary projectile volume taking into account the 10 vol% projectile average content (Table 3). If the estimation of O'Keefe and

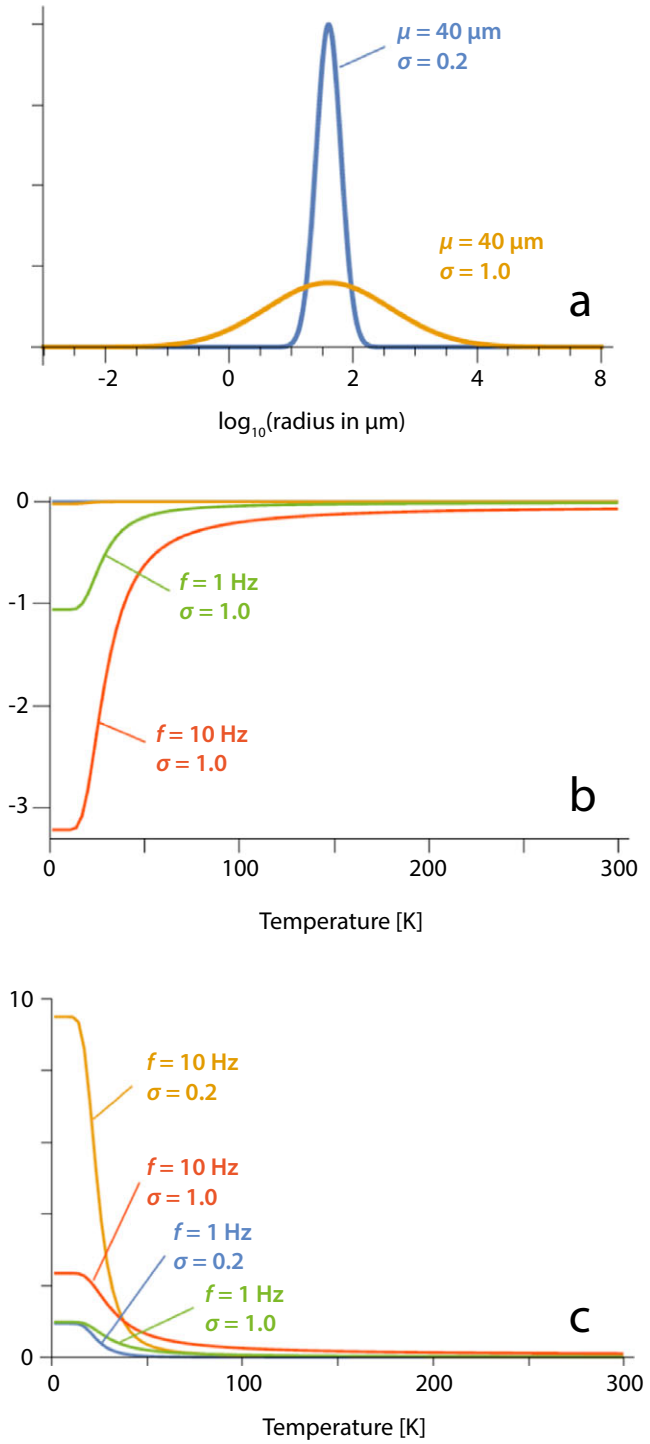

Fig. 10. a) Assumed grain size distribution of Cu spherules. b) In-phase susceptibility of Cu spherules, normalized at 5 K and 1 Hz, mean radius = 40 μm. c) Out-of-phase susceptibility of Cu spherules, normalized at 5 K and 1 Hz, mean radius = 40 μm.

Ahrens (1982) is correct, then some material (melt glass and Cu) was lost or very finely dispersed and not collected.

According to the generalized model of crater growth by Melosh (1989), the penetration and excavation stages are characterized by the flattened projectile spreading on the wall of the growing cavity. The subsurface impact-induced flow of the material of the cavity is nearly completely radial, whereas the flow at margins of the cavity is directed outward forming the early ejecta. We suppose that the flow at the excavation stage is highly turbulent which leads to fine mixing of the dispersed projectile material with the shocked target. Also during crater formation, flow tubes intersect zones of different shock levels. Thus, the ejected particles can contain the projectile material together with the target material fragments with a different degree of shock metamorphism—from molten-state to solid-state shock metamorphosed rocks. Melting of projectile debris can be caused by heat exchange with the target-derived melt and heating during the intense flow of the projectile. Particles with exposed melt on the surface were subsequently decorated by strongly adherent dust. This suggests that the particles at the last stage of their formation were formed in relatively free flight in an ejecta cloud when the melt was not fully solidified.

Glasses and Contamination of Target Material in the Particles by Cu

The "whole rock" homogeneous glasses include numerous projectile droplets. We suggest that their parent melts were formed in the crater cavity at the projectile–target contact surface during the earliest stage of excavation. The contact motion leads to homogenization of the target silicate melt and dissemination of the copper projectile throughout the melt. The heterogeneous and monomineral melts were formed due to high postshock temperatures and originate at a more remote distance from the projectile–target contact than the homogeneous glass. The melt as well as fragments of deeper situated shocked basalt can be incorporated in the homogeneous melt by generation of the agglutinate-like particles.

It has been shown that glasses produced in similar experiments with a steel projectile and silica-rich targets (Ebert et al. 2014) are contaminated by Fe, Cr, V, and other elements, where Fe can be present in the glasses in both oxide and sometimes metallic forms. In the latter case, nanometer-scale metallic Fe inclusions were observed in glasses (Ebert et al. [2014] and fig. 3e therein). We suggest that copper oxidation during the experiments did not take place due to the low atmospheric pressure (Table 1), high shock and postshock temperatures that increase fields of stability for reduced phases on an oxygen fugacity–temperature diagram, and instead expect a

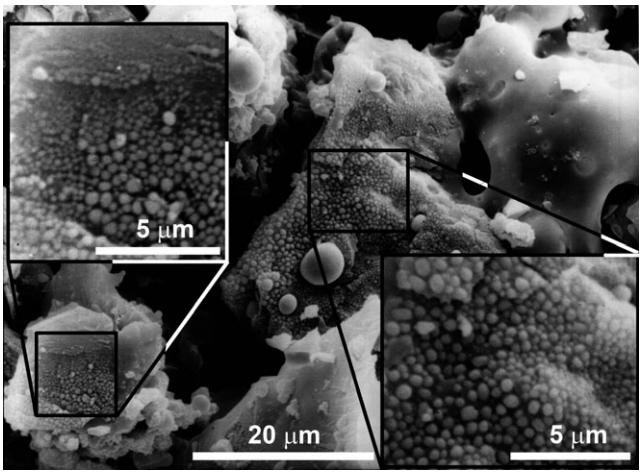

Fig. 11. SE image of agglutinate-like particle surface details (shot 18) illustrating possible Cu vapor condensate on a silicate substrate (plagioclase). Sizes of Cu knobs are systematically changed from larger to smaller in some directions (e.g., for the left upward and for the central upward —to the right). Projectile spraying and dissemination would produce Cu droplets of different sizes (Figs. 2c and 2d).

more conservative behavior of Cu. Hence, the observed strong enrichment of Cu in the homogeneous glasses can be due to the presence of tiny Cu inclusions that are not resolvable on SEM and optical image length scales. As shown above, the Cu contamination of the heterogeneous melt glasses and shocked minerals is not connected with smearing of the projectile matter during preparation of polished sections. There are two mechanisms that may account for the Cu enrichment of the heterogeneous melt glasses and shocked minerals, i.e., (1) diffusion and (2) impregnation of Cu vapor. Shock-induced argon diffusion has been observed in an obsidian sphere loaded by a converging strong shock wave (Badjukov et al. 2000). However, we do not consider diffusion as a mechanism responsible for the Cu enrichment due to the very short duration of the shock compression and the absence of the direct contact of Cu with formation zones of the heterogeneous melt glasses and shocked minerals. Instead, we suggest that high temperatures immediately after pressure release can provoke partial vaporization of copper. High temperatures needed for projectile vaporization can be developed due to its intense plastic flow and heat transfer with a melt at the projectile–target contact. The vapor can impregnate the heterogeneous melt and shocked minerals along fractures and fissures. Evidence of the Cu vapor deposition is shown in Fig. 11, where copper droplets are present on the surface of target fragments.

Comparison to Lunar Agglutinates

Agglutinates in lunar regolith are described as aggregates composed of crystalline grains, glasses, and fragments of older agglutinates bonded together by vesicular glass (Heiken et al. 1991; Basu et al. 2002). Although texturally our experimentally produced agglutinate-like particles are similar to lunar agglutinates, they differ due to (1) presence of copper projectile droplets in the homogeneous glass and (2) relatively low glass content compared with lunar agglutinates. It is accepted that lunar agglutinates were formed by processes of melting and mixing of the melts during impacts of micrometeoroids. The micrometeorite flux is composed almost entirely of chondritic material (Kurat et al. 1994) (mainly CM-like), and hence, it has to be dissolved in target melt by dissemination. Lunar agglutinates contain much more glass compared with the experimentally produced agglutinate-like particles. The reasons for this are silicate compositions of micrometeoroids, repeated impact events, widespread different glasses in regolith, and its porosity; the latter has to result in higher postshock temperatures than in the case of nonporous basaltic target as a result of pore crashing.

Based on the observed similarity between the experimentally produced agglutinate-like particles and lunar agglutinates, we suggest that chondritic content in agglutinates ranges from few percent to 22 vol% with an average of ~10 vol%. Hence, taking into account the iridium (Ir) content in chondrites (~500 ng g^{-1}; Kramar et al. 2001) and ~10% of projectile matter in our agglutinate-like particles, we estimate a mean Ir content in lunar agglutinates as 50 ng g^{-1}. This is a minimum estimate, because of further contributions of a chondritic material in agglutinates by repetitive impacts. It will be interesting to compare our estimates with real values of Ir content in lunar agglutinates, as the element iridium is a known indicator of impact events and abundance of imported undifferentiated matter. To our knowledge, data on Ir content in individual lunar agglutinates are not available at present.

Magnetism of Agglutinate-Like Particles in the Context of the Earth and the Solar System

With only one exception (shot 25), we observed a systematic increase in B_{cr} (two to seven times, see Table 4) for all agglutinate-like particles when compared with the corresponding unshocked basaltic precursors. It is likely to be associated with shock-induced magnetic hardening of the target material, as there was no magnetic contamination of the target by the projectile material (in spite of physical and chemical

mixing between the projectile and the target) due to the nonferrimagnetic (diamagnetic) nature of projectile material. Shock-induced magnetic hardening was reported in previous studies (Cisowski and Fuller 1983; Pesonen et al. 1997; Langenhorst et al. 1999; Gattacceca et al. 2007; Louzada et al. 2008; Bezaeva et al. 2016) and is likely to be linked to shock-induced microfracturing of Tmt grains, the creation of defects, and dislocations in Tmt crystal structures, as well as domain wall pinning (Lindquist et al. 2015). As mentioned above, we also cannot exclude that new SD grains nucleated from the melt, while the initial iron oxide grains have been partially or fully melted, which also has a potential to affect the magnetic hardness of the samples.

Shock-induced magnetic softening (observed on the 4th lithology of tholeiitic basalt, shot 25) was also previously reported in the literature (Bezaeva et al. 2010; Kohout et al. 2012). However, it was explained by either the usage of particularly porous magnetite-bearing targets (Kohout et al. 2012; preshock bulk densities: ~2.1 g cm^{-3}) or shock-induced transformations of ferromagnetic phases (e.g., disorder of tetrataenite into taenite in FeNi-bearing samples due to shock-induced heating in Bezaeva et al. 2010). The 4th lithology of tholeiitic basalt, which demonstrates the effect of shock-induced magnetic softening, was not particularly porous (moreover, its density is the highest of all basalts, see Table 1) and we do not expect any irreversible phase transformations in Tmt due to shock. However, agglutinate-like particles from shot 25 have the highest porosity (20–50 vol%) and may have the highest copper projectile content (up to 21.5 vol%) and high glass content (45–65 vol%). In addition, the basaltic lithology from shot 25 contained Ti-free magnetite, which was somehow destroyed by shock (no traces of Verwey transition characteristic of magnetite in low-temperature magnetic data from agglutinate-like particles from shot 25). All of these observations may be linked to the observed effect.

There is a shock-induced decrease in magnetic susceptibility and saturation magnetization M_s (Table 4) observed in our shock-recovery experiments, which is consistent with previous shock experiments on magnetite targets (Kohout et al. 2012), and the shift of agglutinate-like particles to higher coercivities on the Day plot toward SD endmember compared to their unshocked parent samples (Fig. 7).

Our results have implications for the magnetizations on the surface of the Earth and terrestrial planets, the Moon, and asteroids. Indeed, shock-induced magnetic hardening is likely to be discovered in impact craters on Earth made of basalts, such as Lonar impact crater, India (Louzada et al. 2008). Moreover, basalt is a terrestrial analog of crustal materials of differentiated bodies (e.g., Mars, Moon). Martian crust is known to contain both magnetite (Gattacceca et al. 2014; Wittmann et al. 2015) and titanomagnetite (Bezaeva et al. 2007), as evidenced by the magnetic mineralogy of SNC (Martian) meteorites. Chondritic micrometeoroid bombardment of the magnetite-bearing Martian regolith soil should lead to the formation of agglutinate-like particles similar to the ones described here, because at these conditions, the projectile and target matter behave as liquids during high-velocity impacts. Some differences can be present in particle textures due to melting of chondritic matter and its mixing and dissolution in target melt. Although the agglutination process is unlikely to take place on the Martian surface in such a scale like on the Moon due to the Martian atmosphere, similar shock-induced features, such as impact-induced magnetic hardening of crustal material, are likely to be discovered.

The main carriers of magnetism in lunar materials (both lunar meteorites and returned samples) are metallic iron particles ($\ll$5 wt%) (Rochette et al. 2010). Magnetite was also found in lunar soil, although in negligible quantities ~10^{-6} ppm (Frondel 1975), and undetectable via magnetic methods, which can reveal magnetic minerals in concentrations down to 10 ppm (Rochette et al. 2010). Agglutination and associated magnetic hardening of soil is likely to happen on the surface of the Moon and asteroids with the difference that magnetic properties of the target materials will be equally affected by both shock-induced changes and contamination of surface material by magnetic phases from chondritic projectiles (mainly iron and nickel iron as stated above), which did not take place in our experiments with nonmagnetic (diamagnetic) projectiles. Also the more oxidant atmosphere of the experiment (with respect to vacuum on the Moon) prevented the shock-induced formation of metallic iron.

CONCLUSIONS

Hypervelocity impact experiments (seven independent shots) were conducted using a two-stage light-gas gun with 5 mm-sized spherical copper projectiles sent to four types of basalt targets at ~6 km s^{-1} impact velocities. Shock-recovery experiments resulted in the formation of agglutinate-like particles, which represent a mixture of glass, unmelted basalt target fragments, and copper projectile material. According to pressure estimates, maximum peak pressure in the shock waves ranges from 91 to 132 GPa. Agglutinate-like particles represent a mixture of materials with different shock stages bound together by glass. Unmelted basaltic clasts from all shots were

shocked to a minimum of 25–30 GPa as evidenced by the conversion of plagioclase to diaplectic glass.

Agglutinate-like particles contained two types of glasses. The first type of glass was chemically homogeneous and close in composition to the target basalt. The second type of glass was heterogeneous and had a flow-banded structure. Compositions of the glass bands were similar to compositions of plagioclase and pyroxene. Our shock-recovery experiments allowed estimating the projectile material content in the target basalts as 2–22 vol% with mean value ~10 vol%. This allows assuming the same % of chondritic matter in lunar agglutinates and estimating the iridium content in lunar agglutinates as 50 ng g^{-1}.

Agglutinate-like particles are ~2 to >10 times less magnetic than precursor basalts and are generally magnetically harder than the corresponding target basaltic precursors. Shock-induced magnetic hardening (increase in B_{cr} in two to seven times) of target materials is consistent with previous shock experiments with targets of basalt-like densities. On the other hand, we cannot exclude that new SD grains have nucleated independently from the melt while primary volcanic oxides have not been entrained in the melt or been fully melted. Possible implications of our results for terrestrial impact craters formed in basalts, as well as for the Moon and other airless solid solar system bodies such as asteroids are discussed above.

Acknowledgments—We thank the anonymous reviewer for the review and constructive suggestions and Prof. Oliver Tschauner for useful suggestions and the editorial handling, which helped to improve the manuscript. The work is supported by Act 211 Government of the Russian Federation, agreement no. 02.A03.21.0006 and is performed according to the Russian Government Program of Competitive Growth of Kazan Federal University. We gratefully acknowledge support by the U.S. National Science Foundation IRM Visiting Fellowship to N.S.B. D.D.B. was supported by Program no. 7P of Presidium RAS and a Russian Science Foundation Grant 17-17-01279. D.D.B. acknowledges the staff at the Center of Microscopy and Nanotechnology of the University of Oulu (Finland) for assistance with some aspects of electron microprobe and SEM works.

Editorial Handling—Dr. Oliver Tschauner

REFERENCES

Ahrens T. J. 1993. Equation of state. In *High-pressure shock compression of solids*, edited by Asay J. R. and Shahinpoor M. New York: Springer-Verlag. pp. 75–114.

Ahrens T. J. and Johnson M. L. 1995a. Shock wave data for minerals. In *Mineral physics and crystallography: A handbook of physical constants*, edited by Ahrens T. J. Washington, D.C.: American Geophysical Union. pp. 143–175.

Ahrens T. J. and Johnson M. L. 1995b. Shock wave data for rocks. In *Rock physics and phase relations: A handbook of physical constants*, edited by Ahrens T. J. Washington, D.C.: American Geophysical Union. pp. 35–44.

Ahrens T. J. and O'Keefe J. D. 1977. Equation of state and impact-induced shock-wave attenuation on the moon. In *Impact and explosion cratering*, edited by Roddy D. J., Pepin R. O., and Merril R. B. New York: Pergamon Press. pp. 639–656.

Badjukov D. D., Kozlov E. A., Kolesnikov E. M., Lebedeva L. M., and Nazarov M. A. 2000. Behavior of ^{40}Ar in obsidian subjected to strong shock-wave compression. *Doklady RAS, Earth Sciences* 373:905–908. (in Russian)

Basu A., Wentworth S. J., and McKay D. S. 2002. Heterogeneous agglutinitic glass and the fusion of the finest fraction (F^3) model. *Meteoritics & Planetary Science* 37:1835–1842.

Bezaeva N. S., Rochette P., Gattacceca J., Sadykov R. A., and Trukhin V. I. 2007. Pressure demagnetization of the Martian crust: Ground truth from SNC meteorites. *Geophysical Research Letters* 34:L23202.

Bezaeva N. S., Badjukov D. D., Rochette P., Gattacceca J., Trukhin V. I., Kozlov E. A., and Uehara M. 2010. Experimental shock metamorphism of the L4 ordinary chondrite Saratov induced by spherical shock waves up to 400 GPa. *Meteoritics & Planetary Science* 45:1007–1020.

Bezaeva N. S., Swanson-Hysell N. L., Tikoo S. M., Badyukov D. D., Kars M., Egli R., Chareev D. A., Fairchild L. M., Khakhalova E., Strauss B. E., and Lindquist A. K. 2016. The effect of 10 to >160 GPa shock on the magnetic properties of basalt and diabase. *Geochemistry, Geophysics, Geosystems* 17:4753–4771.

Bischoff A., Scott E. R. D., Metzler K., and Goodrich C. A. 2006. Nature and origin of meteoritic breccias. In *Meteorites and the early solar system II*, 2nd ed., edited by Lauretta D. S. and McSween H. Y. Jr. Tucson, Arizona: The University of Arizona Press. pp. 679–712.

Bleil U. and Petersen N. 1982. Magnetic properties of natural minerals. In *Numerical data and functional relationships in science and technology, group V: Geophysics and space research*, edited by Angenheister G. New York: Springer. pp. 308–365.

Bouhifd M. A., Besson P., Courtial P., Gérardin C., Navrotsky A., and Richet P. 2007. Thermochemistry and melting properties of basalt. *Contributions to Mineralogy and Petrology* 153:689–698.

Bowles J., Jackson M., Chen A., and Solheid P. 2009. Interpretation of low-temperature data part 1: Superparamagnetism and paramagnetism. *The IRM Quarterly* 19:1, 7–11.

Carter-Stiglitz B., Moskowitz B., Solheid P. Berquo T. S., Jackson M., and Kosterov A. 2006. Low-temperature magnetic behavior of multidomain titanomagnetites: TM0, TM16, and TM35. *Journal of Geophysical Research* 111: B12S05.

Church N., Feinberg J. M., and Harrison R. 2011. Low-temperature domain wall pinning in titanomagnetite: Quantitative modeling of multidomain first-order reversal

curve diagrams and AC susceptibility. *Geochemistry, Geophysics, Geosystems* 12:Q07Z27.
Cintala M. J., Hörz F., See T. H., Cardenas F., and Thompson T. D. 1984. Regolith evolution experiments I: Grain-size evolution (abstract). 15th Lunar and Planetary Science Conference. p. 160.
Cisowski S. M. and Fuller M. 1983. The role of impact magnetization in the solar system. *Advances in Space Research* 2:35–39.
Cremonese G., Borin P., Lucchetti A., Marzari F., and Bruno M. 2013. Micrometeoroids flux on the Moon. *Astronomy & Astrophysics* 551:A27.
Day R., Fuller M. D., and Schmidt V. A. 1977. Hysteresis properties of titanomagnetites: Grain size and composition dependence. *Physics of the Earth and Planetary Interiors* 13:260–266.
Dunlop D. J. 2002. Theory and application of the Day plot (Mrs/Ms versus Hcr/Hc) 1. Theoretical curves and tests using titanomagnetite data. *Journal of Geophysical Research* 107:EPM 4-1–EPM 4-22.
Dunlop D. J. and Özdemir Ö. 1997. *Rock magnetism, fundamentals and frontiers*. Cambridge: Cambridge University Press. 573 p.
Ebert M., Hecht L., Deutsch A., Kenkmann T., Wirth R., and Berndt J. 2014. Geochemical processes between steel projectiles and silica-rich targets in hypervelocity impact experiments. *Geochimica et Cosmochimica Acta* 133:257–279.
Egli R. 2013. VARIFORC: An optimized protocol for the calculation of non-regular first-order reversal curve (FORC) diagrams. *Global and Planetary Change* 110:302–320.
Frondel J. W. 1975. *Lunar mineralogy*. New York: Wiley-Interscience. 332 p.
Garcia R. F., Murdoch N., and Mimoun D. 2015. Micro-meteoroid seismic uplift and regolith concentration on kilometric scale asteroids. *Icarus* 253:159–168.
Gattacceca J., Lamali A., Rochette P., Boustie M., and Berthe L. 2007. The effects of explosive-driven shocks on the natural remanent magnetization and the magnetic properties of rocks. *Physics of the Earth and Planetary Interiors* 162:85–98.
Gattacceca J., Rochette P., Scorzelli R. B., Munayco P., Agee C., Quesnel Y., Cournede C., and Geissman J. 2014. Martian meteorites and Martian magnetic anomalies: A new perspective from NWA 7034. *Geophysical Research Letters* 41:4859–4864.
Grommé C. S., Wright T. L., and Peck D. L. 1969. Magnetic properties and oxidation of iron-titanium oxide minerals in Alae and Makaopuhi lava lakes, Hawaii. *Journal of Geophysical Research* 74:5277–5293.
Harrison R. J. and Feinberg J. M. 2008. FORCinel: An improved algorithm for calculating first-order reversal curve (FORC) distributions using locally-weighted regression smoothing. *Geochemistry, Geophysics, Geosystems* 9:Q05016.
Heiken G. H., Vaniman D. T., and French B. M., eds. 1991. *Lunar sourcebook: A user's guide to the moon*. Cambridge: Cambridge University Press. 736 p.
Hörz F. and Cintala M. 1997. Impact experiments related to the evolution of planetary regoliths. *Meteoritics & Planetary Science* 32:179–209.
Hörz F. and Schaal R. B. 1981. Asteroidal agglutinate formation and implications for asteroidal surfaces. *Icarus* 46:337–353.
Hörz F., Brownlee D. E., Fechtig H., Hartung J. B., Morrison D. A., Neukum G., Schneider E., Vedder J. F., and Gault D. E. 1975. Lunar microcraters: Implications for the Micrometeoroid complex. *Planetary and Space Science* 23:151–172.
Jackson M., Moskowitz B., and Bowles J. 2011. Interpretation of low-temperature data part III: The magnetite Verwey transition (Part A). *The IRM Quarterly* 20:1, 7–11.
Kohout T., Pesonen L. J., Deutsch A., Wunnemann K., Nowka D., Hornemann U., and Heikinheimo E. 2012. Shock experiments in range of 10–45 GPa with small multidomain magnetite in porous targets. *Meteoritics & Planetary Science* 47:1671–1680.
Korotev R. L., Zeigler R. A., and Floss C. 2010. On the origin of impact glass in the Apollo 16 regolith. *Geochimica et Cosmochimica Acta* 74:7362–7388.
Kramar U., Stüben D., Berner Z., Stinnesbeck W., Philipp H., and Keller G. 2001. Are Ir anomalies sufficient and unique indicators for cosmic events. *Planetary and Space Science* 49:831–837.
Kurat G., Koeberl C., Presper T., Brandstätter F., and Maurette M. 1994. Petrology and geochemistry of Antarctic micrometeorites. *Geochimica et Cosmochimica Acta* 58:3879–3904.
Kyte F. T. and Wasson J. T. 1986. Accretion rate of extraterrestrial matter: Iridium deposited 33 to 67 million years ago. *Science* 232:1225–1229.
Langenhorst F., Pesonen L. J., Deutsch A., and Hernemann U. 1999. Shock experiments on diabase: Microstructural and magnetic properties (abstract #1241). 30th Lunar and Planetary Science Conference. CD-ROM.
Lindquist A. K., Feinberg J. M., Harrison R. J., Loudon J. C., and Newell A. J. 2015. Domain wall pinning and dislocations: Investigating magnetite deformed under conditions analogous to nature using transmission electron microscopy. *Journal of Geophysical Research: Solid Earth* 120:1415–1430.
Linford N., Jackson M., and Marvin J. 2002. Seahenge, susceptibility and more ways to be wrong. *The IRM Quarterly* 12:1, 10–11.
Louzada K. L., Weiss B. P., Maloof A. C., Stewart S. T., Swanson-Hysell N. L., and Soule A. 2008. Paleomagnetism of Lonar impact crater, India. *Earth and Planetary Science Letters* 275:308–319.
Love S. G. and Brownlee D. E. 1993. A direct measurement of the terrestrial mass accretion rate of cosmic dust. *Science* 262:550–553.
McQueen R. G. and Marsh S. P. 1960. Equation of state for nineteen metallic elements from shockwave measurements to two megabars. *Journal of Applied Physics* 31:1253–1269.
Melosh H. J. 1989. *Impact cratering: A geologic process*. New York: Oxford University Press. p. 253.
Morris R. V. and Gose W. A. 1976. Ferromagnetic resonance and magnetic studies of cores 60009/60010 and 60003—Compositional and surface-exposure stratigraphy. Proceedings, 7th Lunar Science Conference. pp. 1–11.
Noguchi T., Kimura M., Hashimoto T., Konno M., Nakamura T., Zolensky M. E., Okazaki R., Tanaka M., Tsuchiyama A., Nakato A., Ogami T., Ishida H., Sagae R., Tsujimoto S., Matsumoto T., Matsuno J., Fujimura A., Abe M., Yada T., Mukai T., Ueno M., Okada T., Shirai K., and Ishibashi Y. 2014. Space weathered rims found on the surfaces of the Itokawa

dust particles. *Meteoritics & Planetary Science* 49:188–214.

O'Keefe J. D. and Ahrens T. J. 1982. Cometary and meteorite swarm impact on planetary surfaces. *Journal of Geophysical Research* 87:6668–6680.

Ostertag R. 1983. Shock experiments on feldspar crystals. Proceedings, 14th Lunar and Planetary Science Conference. pp. B364–B376.

Papike J. J. 1981. The lunar regolith: significance of the chemistry of the < 10 μm fraction and a model for agglutinate formation involving fusion of the finest fraction (F^3). Proceedings, 12th Lunar and Planetary Science Conference. pp. 851–853.

Pesonen L. J., Deutsch A., Hornemann U., and Langenhorst F. 1997. Magnetic properties of diabase samples shocked experimentally in the 4.5 to 35 GPa range (abstract #1370). 28th Lunar and Planetary Science Conference. CD-ROM.

Rochette P., Gattacceca J., Ivanov A. V., Nazarov M. A., and Bezaeva N. S. 2010. Magnetic properties of lunar materials: Meteorites, Luna and Apollo. *Earth and Planetary Science Letters* 292:383–391.

Rochette P., Gattacceca J., Devouard B., Moustard F., Bezaeva N. S., Cournède C., and Scaillet B. 2015. Magnetic properties of tektites and other related impact glasses. *Earth and Planetary Science Letters* 432:381–390.

Schaal R. B., Thompson T. D., Hörz F., and Bauer J. F. 1979. Shock metamorphism of granulated lunar basalt. Proceedings, 10th Lunar and Planetary Science Conference. pp. 2547–2571.

See T. and Hörz F. 1988. Formation of agglutinate-like particles in an experimental regolith. Proceedings, 18th Lunar and Planetary Science Conference. pp. 423–433.

Stuart J. S. and Binzel R. P. 2004. Bias-corrected population, size distribution, and impact hazard for the near-Earth objects. *Icarus* 170:295–311.

Taylor L. A., Pieters C., Keller L. P., Morris R. V., McKay D. S., Patchen A., and Wentworth S. 2001. The effects of space weathering on Apollo 17 mare soils: Petrographic and chemical characterization. *Meteoritics & Planetary Science* 36:285–299.

Van de Moortèle B., Reynard B., Rochette P., Jackson M., Beck P., Gillet P., and McMillan P. F. 2007. Shock-induced metallic iron nanoparticles in olivine-rich Martian meteorites. *Earth and Planetary Science Letters* 262:37–49.

Verwey E. J. W. 1939. Electronic conduction of magnetite (Fe_3O_4) and its transition point at low temperatures. *Nature* 144:327–328.

Wittmann A., Korotev R. L., Jolliff B. L., Irving A. J., Moser D. E., Barker I., and Rumble D. 2015. Petrography and composition of Martian regolith breccia meteorite Northwest Africa 7475. *Meteoritics & Planetary Science* 50:326–352.

Worm H.-U., Clark D., and Dekkers M. J. 1993. Magnetic susceptibility of pyrrhotite: Grain size, field and frequency dependence. *Geophysical Journal International* 114:127–137.